



Geochemistry, Geophysics, Geosystems

RESEARCH ARTICLE

10.1002/2016GC006687

Shear localization in a mature mylonitic rock analog during fast slip

M. Takahashi¹, M. P. A. van den Ende² , A. R. Niemeijer² , and C. J. Spiers²
¹Geological Survey of Japan, National Institute of Advanced Industrial Science and Technology, Tsukuba, Japan, ²High Pressure and Temperature Laboratory, Faculty of Geosciences, Utrecht University, Utrecht, Netherlands

Key Points:

- We investigated the frictional response of analog gouge with a mature mylonitic microstructure
- The direct response to a velocity step decreases strongly when the poststep velocity exceeds 20 $\mu\text{m/s}$
- Once a mylonitic structure has developed, deformation at high velocity tends to be localized

Correspondence to:

M. Takahashi,
miki.takahashi@aist.go.jp

Citation:

Takahashi, M., M. P. A. van den Ende, A. R. Niemeijer, and C. J. Spiers (2017), Shear localization in a mature mylonitic rock analog during fast slip, *Geochem. Geophys. Geosyst.*, 18, 513–530, doi:10.1002/2016GC006687.

Received 19 OCT 2016

Accepted 5 JAN 2017

Accepted article online 10 JAN 2017

Corrected 3 FEB 2017

This article was corrected on 25 FEB 2017. See the end of the full text for details.

Abstract Highly localized slip zones developed within ductile shear zones, such as pseudotachylyte bands occurring within mylonitic fabric rocks, are frequently interpreted as evidence for earthquake nucleation and/or propagation within the ductile regime. To understand brittle/frictional shear localization processes in ductile shear zones and to relate these to earthquake nucleation and propagation, we performed tests with large changes in velocity on a brine-saturated, 80:20 (wt %) mixture of halite and muscovite gouge after forming a mature mylonitic structure through frictional-viscous flow. The direct effect a on shear strength that occurs in response to an instantaneous upward velocity-step is an important parameter in determining the nature of seismic rupture nucleation and propagation. We obtained reproducible results regarding low-velocity mechanical behavior compared with previous work, but also obtained new insights into effects of sudden increases in slip velocity on localization and strength evolution, at velocities above a critical velocity V_c ($\sim 20 \mu\text{m/s}$). We found that once a ductile, mylonitic structure has developed in a shear zone, subsequent cataclastic deformation is consistently localized in a narrow zone. This switch to localized deformation is controlled by the imposed velocity and becomes most apparent at velocities above V_c . In addition, the direct effect drops rapidly when the velocity exceeds V_c . This implies that slip can accelerate toward seismic velocities almost instantly and without much loss of fracture energy, once V_c is exceeded. Obtaining a measure for V_c in natural faults is therefore of key importance for understanding earthquake nucleation and propagation in the brittle-ductile transitional regime.

1. Introduction

Earthquake nucleation and propagation in the Earth involve the acceleration of slip on a fault toward meter per second values from a background, quasi-static, low-velocity state enough to be regarded as locked state. It is believed that during a seismic slip event, cataclastic processes, involving rapid grain comminution and frictional heating, play a dominant role at the microscale [e.g., Sibson, 2003], sometimes forming frictional melts which are preserved as pseudotachylytes that provide a tangible record of the event [e.g., Sibson, 1975; Niemeijer et al., 2012; Di Toro et al., 2006]. Commonly, pseudotachylytes are found to have formed under pressure and temperature (P-T) conditions that favor ductile deformation such as crystal plastic and/or diffusion creep [e.g., Kilian et al., 2011; Holdsworth et al., 2001] at certain depths [e.g., Sibson, 1980; Hobbs et al., 1986; Takagi et al., 2000; Handy et al., 2007; Lin, 2008; Jianga et al., 2015]. Mylonitic fabric rocks (a term used loosely here to refer to a deformed rock with a S-C and/or -C' fabric at quasi-static strain rates ($<10^{-10} \text{ s}^{-1}$ or $\sim 1 \text{ nm/s}$) resulting from a ductile deformation mechanism) contain deformation features formed under high-temperature and pressure conditions that characterize deep fault creep occurring between seismic events. This means that the pressure and temperature conditions at which mylonitic structures form during the aseismic stage also allow for the nucleation or propagation of frictional instabilities, i.e., earthquakes, during the coseismic stage. This in turn raises the question how mylonitic rock will behave in response to slip-acceleration after being subjected to low strain rates over a longer period of time, allowing ductile structures to fully mature. Does the fault still exhibit classical rate- and state-behavior as was found by Dieterich [Dieterich, 1972, 1978, 1979], and if so, are the values of the frictional parameters still the same as those obtained in low-velocity friction experiments by imposing the $1/2$ to 1-order velocity steps typically used in friction experiments?

Laboratory friction experiments employing velocity steps are a useful tool for assessing the potential for unstable sliding of a fault gouge (or bare rock surface) subject to an imposed set of conditions. A criterion for the stability of sliding can be determined by assessing the sign of $a-b$, where a and b are the rate and

state frictional parameters, derived from the following law (hereafter referred to as RSF law) [Dieterich, 1978; Ruina, 1983]:

$$\frac{\tau(V, \theta)}{\sigma_n} = \mu(V, \theta) = \mu^* + a \ln \left(\frac{V}{V^*} \right) + b \ln \left(\frac{\theta}{\theta^*} \right), \quad (1)$$

where τ , σ_n , and μ are shear stress, (effective) normal stress, and friction coefficient, and V and θ are the sliding velocity and state variable, respectively. μ^* is the friction coefficient at the reference state at velocity V^* and state variable θ^* ($=D_c/V^*$, with D_c being a characteristic displacement for the evolution). The parameter a (the direct effect) is the instantaneous change in friction coefficient as a result of a log-step change in velocity, and b (the evolution effect) is the gradual change in friction coefficient followed by such a step. Negative values of $(a-b)$ indicate velocity-weakening and potentially unstable sliding, while positive values indicate velocity-strengthening and stable sliding.

From the experiments, the frictional characteristics of the sample can be quantified in terms of rate and state parameters which can then serve as input for numerical earthquake simulations [e.g., Lapusta *et al.*, 2000; Lapusta and Rice, 2003; Noda *et al.*, 2013]. However, due to technical limitations of many laboratory experiments, it is nontrivial to obtain slip acceleration in initially mylonitic structured rocks developed gradually at quasi-static strain rates or sliding velocities. Generally, frictional behavior has typically been tested (1) using 1 or half-order of magnitude changes in sliding velocity, (2) using initially noncoherent powdered minerals, (3) at velocity, pressure, and temperature conditions where frictional behavior dominates the overall rheology, and (4) attaining insufficient strain to fully mature the microstructure, especially in experiments on materials subjected to low-velocity and high-temperature conditions that are in principle capable of producing mylonitic structures.

In order to tackle these issues, we conducted experiments on a fault rock analog material (halite-muscovite mixture) imposing large steps in velocity after a mature mylonitic structure had formed at low velocity. The low velocity, mylonitic microstructure is easily obtained in this analog material, even at ambient laboratory conditions. The characteristics of the analog system have been extensively studied in previous work [e.g., Bos and Spiers, 2000; Niemeijer and Spiers, 2005, 2006, 2007]. Following up on previous experiments by Niemeijer and Spiers [2006], the choice was made for a brine-saturated, 80:20 (wt %) mixture of halite and muscovite, which displays significant variations in shear strength and microstructure within the range of sliding velocities (0.03–13 $\mu\text{m/s}$) that is easily attainable in the laboratory [see Niemeijer and Spiers, 2005, Figure 10].

At the lower velocities investigated ($<1 \mu\text{m/s}$), Niemeijer and Spiers found that a mylonitic structure formed in association with velocity-strengthening behavior, due to a combination of pressure solution creep of halite grains plus frictional sliding on or within the muscovite foliation. At high velocities, the material was found to weaken significantly with increasing sliding velocity, and a chaotic and porous structure would form within the gouge layer [Niemeijer and Spiers, 2006]. Those earlier experiments focused on the steady state shear strength related to the microstructures at constant velocity at relatively low velocity. Here in our experiments we explore the effects of large variations in slip velocity on the evolution of friction and corresponding microstructure. In particular, we focus on the frictional behavior of simulated fault gouges and the associated shear-localization that occurs when relatively high-velocity slip is imposed on a pre-existing mylonitic structure formed at low strain rates.

2. Method

2.1. Sample Material and Apparatus

The experiments were performed on a simulated gouge consisting of a mixture of 80 wt % analytical grade halite, crushed and sieved to a grain size $<75 \mu\text{m}$, and 20 wt % muscovite (grain size $<44 \mu\text{m}$). The sample material was prepared and stored in a low-humidity ($<25\%$ RH) room to prevent adsorption of water. Approximately 5 g of this material was then sandwiched between two toothed, hardened-steel piston rings, forming a 1–2 mm thick layer. The piston rings had an inner diameter of 80 mm, and an outer diameter of 98 mm (Figure 1a), with the teeth being approximately 0.2 mm in height (Figure 1b). The rings have inner and outer grooves accommodating four O-rings that prevent fluid from leaking. The assembly was radially confined by inner and outer stainless steel sealing rings, with a pore-fluid inlet and outlet housed in the outer sealing ring. Fluid inlet and outlet ports were anytime open to keep drainage condition. The assembly

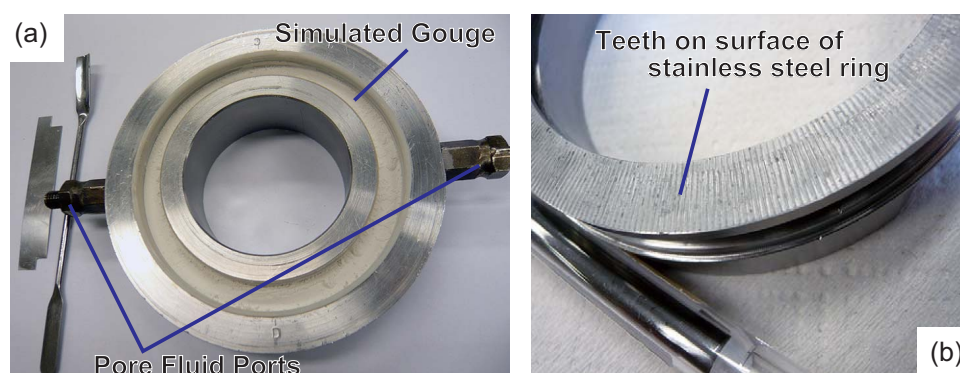


Figure 1. (a) Photograph of the specimen assembly. A powder of simulated gouge mixture (4.0 g of halite and 1.0 g of muscovite) was placed between the stainless steel rings. The sliding surface of the piston has an inner diameter of 80 and a 98 mm outer diameter. (b) An enlarged view of the surface of the stainless steel ring, which is grooved to impede localization of deformation on the steel-gouge interface. The scale (a pen, bottom left) is 9 mm in diameter.

was then mounted into a rotary shear apparatus, situated in an Instron 1362 loading frame [Bos and Spiers, 2000; Niemeijer and Spiers, 2005, 2006, 2007]. The loading frame applied a constant, servo-controlled normal force, accurate within approximately 0.01 kN, while a servo-controlled drive system was used to apply a rotational sliding velocity. Shear load was measured by a pair of load cells (~ 5 kPa in resolution) mounted in a torque couple at the upper side of the stationary forcing block. In order to facilitate a certain sliding velocity range, different gear box and motor arrangements were used. Each arrangement allowed for a velocity range spanning approximately 4 orders of magnitude, with the lowest attainable velocity being 1 nm/s, and the highest 1 cm/s. The tangential displacement was measured with a potentiometer of 4 μ m resolution, normal displacements (i.e., dilatation and compaction of the sample) were measured with an LVDT (0.01% resolution over 1 mm full scale) attached to the side of the forcing block and the loading frame. However, we could not use the LVDT data to accurately calculate instantaneous dilation/compaction rates of the gouge during a step toward high velocities, because the LVDT response is somewhat delayed and attenuated. Data were acquired at a rate of 0.9 kHz, but down-sampled to a rate varying from 1 to 300 Hz depending on the (imminent) sliding rate.

2.2. Procedure

All samples were loaded to 5 MPa normal stress, at ambient conditions (21–25°C, up to 80% RH). Then, brine was introduced using a constant flow rate syringe pump, and after saturation was achieved, the sample was allowed to compact over a 1–3 h time period. After precompaction, the sample was sheared for 10 mm at a load-point velocity of $V_0 = 10$ μ m/s (or 25 μ m/s for experiment u253) to achieve a similar starting microstructure for all experiments. Then, the velocity was changed to the initial target velocity V_1 and maintained at this for displacements of at least 15 mm, which are sufficient to obtain a fully matured microstructure. Subsequently, a velocity-step to the final velocity V_2 was imposed and maintained over 10 mm displacement (for the cases at $V_2 = 1$ cm/s, V_2 for sliding was maintained over 100 mm in displacement since D_c might be relatively longer to obtain the steady state shear stress), and the experiment was terminated.

At the end of each experiment, shear load was removed by reversing the rotation direction of the machine until shear load became zero before unloading the normal force, to prevent uncontrolled slip on the sample. As soon as possible after removal of the normal load, the residual brine in the specimen was flushed out with n-hexane to avoid deposition of halite [Niemeijer and Spiers, 2006], and the sample was dried in an oven at 50°C for a half-day. Then, pieces of the specimen were impregnated with epoxy resin. Thin sections cut parallel to the sliding direction were prepared with silicon carbide and alumina abrasives under dry conditions.

In addition to the single-step experiments, velocity-stepping experiments were conducted with several smaller velocity steps (half and 1 order in magnitude) for comparison with the single, larger velocity steps. All data were analyzed by fitting the RSF law (1) following the aging law with two state variables [Dieterich, 1979; Ruina, 1983] to the data set, using the Levenberg-Marquardt least squares algorithm [Noda and Shimamoto, 2009; Takahashi et al., 2011]. However, since the largest jumps in velocity required up to 0.5 s

to accelerate toward the target velocity, the velocity step could no longer be considered to be instantaneous and the RSF equations had to be modified to allow for a gradual change in driving velocity (see Appendix for details). All experimental conditions and results are listed in Table 1.

3. Results

3.1. Steady State Strength

It was found that the steady state shear strengths τ_{ss} obtained in our experiments was in good agreement with those observed by *Niemeijer and Spiers* [2006] (Figure 2). This demonstrates the good reproducibility of the method and suggests that the steady state strength is not strongly affected by the deformation history of the sample. Based on our data, we define three regimes of frictional behavior: a velocity-strengthening regime at low velocities (R-1, $V < 1 \mu\text{m/s}$), a velocity-weakening regime at intermediate velocities (R-2, $1 < V < 20 \mu\text{m/s}$), and a velocity-neutral regime at the highest velocities (R-3, $V > 20 \mu\text{m/s}$) (see Figure 2).

3.2. Rate and State Frictional Behavior

The transient frictional behavior of the gouge following a large step up in velocity (Figure 3) could generally be modeled very well by the standard RSF law [*Dieterich*, 1979]. We adopted the aging law as the evolution law. Figure 3 shows the transient behaviors upon stepping up to a constant $V_2 = 1.02 \text{ mm/s}$ from different V_1 (3a: $0.18 \mu\text{m/s}$, 3b: $0.96 \mu\text{m/s}$, and 3c: $5.00 \mu\text{m/s}$). Calculated direct effects indicated a decreasing with increasing V_1 . However, in two cases we did not succeed in fitting the RSF law to the data (Figure 4). In the first case (u242; $V_1 = 0.03 \mu\text{m/s}$, $V_2 = 10.17 \mu\text{m/s}$; Figure 4a), the peak shear stress and rapid subsequent drop was not captured well by the RSF law. The pronounced yield point, here at 5.7 MPa ($\tau/\sigma_n = 1.14$), was not observed in other velocity step tests. In the second case (u239 and u253; both $V_2 = 1 \text{ cm/s}$; Figure 4b), no direct effect was recorded. Hereafter, we report the RSF parameters for u242 obtained from the inversion, but note that these values are only indicative for the approximate magnitude of the direct effect. For the experiments with $V_2 = 1 \text{ cm/s}$, we consider the direct effect to be zero.

The transient behavior for velocity steps reaching V_2 values beyond a critical velocity of $20 \mu\text{m/s}$, i.e., steps crossing the boundary between the velocity-weakening regime (R-2) and the velocity-neutral regime (R-3), was very different from that produced by smaller velocity steps (Figure 5). Generally, the instantaneous increase of the shear stress in response to a change in velocity was significantly smaller in the large step tests than in the small step cases, except for u242 (Figure 4a), which was conducted at our lowest V_1 ($=0.03 \mu\text{m/s}$). This observation provides several new perspectives on frictional behavior during earthquake nucleation and propagation. Figure 5a displays the strength-log velocity evolution paths, calculated by means of the nonlinear least squares fitting technique (Appendix A), connecting τ_{ss} at V_1 (red circle) to τ_{ss} at V_2 (blue circle) for each velocity-stepping experiment. The paths or traces represented by green and purple-colored lines reflect half and 1-order velocity steps performed in the multistep experiment. The apparent linear increase of the shear strength from τ_{ss} at V_1 (red circle), per decade of velocity increase along the traces, is proportional to the direct effect parameter a , corresponding to $a \cdot \sigma_n / \log e$ as drawn in Figure 5a, as $a = (\text{instantaneous change in the shear strength}) \cdot (V/\Delta V)/\sigma_n$. We observed a common trend that the direct effect a decreases with increasing V_1 , and approaches zero at $V_1 > 20 \mu\text{m/s}$, for both the single-step and multistep experiments (Figure 5b). Finally, the direct effect vanishes when both V_1 and V_2 are relatively high (see Figure 4b: $V_1 = 15 \mu\text{m/s}$ and $V_2 = 1 \text{ cm/s}$). Additionally, we observed differences in the values of a obtained in experiments at $V_2 > 20 \mu\text{m/s}$ versus those at $V_2 < 20 \mu\text{m/s}$, even though V_1 was constant: the direct effect was significantly smaller for cases where $V_2 > 20 \mu\text{m/s}$ than for those where $V_2 < 20 \mu\text{m/s}$.

The direct effect thus varies with both V_1 and V_2 , suggesting a velocity-history dependence (i.e., a dependence on the foregoing sequence of imposed velocities). The key velocity in our study lies around $20 \mu\text{m/s}$, which marks the boundary between the R-2 and R-3 velocity regimes. Additionally, it was found that τ_{ss} is independent of the velocity history, making the evolution effect b a “dependent variable” in the relationship $b = a - \Delta\tau_{ss}/\sigma_n \ln(V_2/V_1)$, where $\Delta\tau_{ss} = \tau_{ss}(V_2) - \tau_{ss}(V_1)$.

3.3. Microstructures

Fragments derived from the deformed gouge layer were sectioned and dry-polished for microstructural analysis. We compare the microstructural observations with those reported by [*Niemeijer and Spiers*, 2005, 2006, 2007]. In the velocity-strengthening regime (R-1) at $V < 1 \mu\text{m/s}$, these authors found mylonitic

Table 1. Summary of the Experiments and Results of the Nonlinear Least Squares Curve Fitting to the Data Obtained in the Velocity Step Tests

Experiment No.	History of Velocity			Steady State Shear Strength		RSF Parameters Obtained by Nonlinear Least Squares Curve Fitting ($\pm 2SE$)										Remarks
	Gear and Motor ^a	V ₁ (μm/s)	V ₂ (μm/s)	Displ. for V ₁ (μm)	τ _{ss} at V ₁ (MPa)	τ _{ss} at V ₂ (MPa)	α	a	b ₁	b ₂	DC ₁ (μm)	DC ₂ (μm)	k (μm)	R ²		
Large V Step Tests																
u237	Set-B	0.18	1020.60	11.6	3.05	1.65	15.31 ± 0.06	0.02335 ± 0.00016	0.03604 ± 0.00040	0.02083 ± 0.00038	161.104 ± 1.232	406.837 ± 3.858	0.00094 ± 0.00002	0.9978	Figure 3a	
u238	Set-B	0.17	1019.50	26.6	2.85	1.48	17.53 ± 0.02	0.02182 ± 0.00006	0.02651 ± 0.00026	0.02076 ± 0.00026	163.794 ± 0.820	335.468 ± 1.650	0.00093 ± 0.00001	0.9990	Figure 6a–6c and A1	
u239	Set-C	15.32	10540.00	68.2	1.71	1.25	~0								^c Figures 4b and 8c	
u241	Set-B	1.90	1021.20	31.0	3.17	1.37	15.61 ± 0.06	0.01136 ± 0.00012	0.03265 ± 0.00060	0.02543 ± 0.00060	212.195 ± 2.252	477.308 ± 4.998	0.00074 ± 0.00001	0.9964		
u242	Set-A	0.03	10.17	19.6	2.17	2.09	9.39 ± 0.18	0.18540 ± 0.00070	0.12050 ± 0.00086	0.05779 ± 0.00082	18.052 ± 0.237	72.560 ± 0.704	0.00493 ± 0.00002	0.9853	^c Figures 4a and 7c	
u244	Set-B	5.00	1020.20	19.5	2.76	1.38	13.97 ± 0.12	0.00426 ± 0.00012	0.03454 ± 0.00022	0.01725 ± 0.00020	288.987 ± 2.148	1038.334 ± 8.132	0.00211 ± 0.00006	0.9962	Figures 3c, 6f, and 6g	
u249	Set-B	0.93	1021.90	18.5	3.40	1.58	16.42 ± 0.02	0.01013 ± 0.00012	0.02937 ± 0.00076	0.03215 ± 0.00066	219.985 ± 2.432	422.189 ± 3.542	0.00074 ± 0.00002	0.9986	Figures 3b, 6d, and 6e	
Small V Step Tests																
u243	Set-B	0.91	2.93	13.5	3.35	3.36	10.03 ± 0.50	0.11724 ± 0.00028	0.08053 ± 0.00026	0.06283 ± 0.00020	57.208 ± 0.380	410.291 ± 2.580	0.00540 ± 0.00002	0.9975		
		2.93	10.10	4.4	3.36	2.80	10.00 ± 0.28	0.06372 ± 0.00084	0.07741 ± 0.00086	0.07432 ± 0.00028	71.266 ± 1.176	1278.072 ± 7.824	0.00601 ± 0.00022	0.9838		
		10.10	30.53	6.1	2.80	2.27	13.94 ± 0.16	0.01722 ± 0.00020	0.03522 ± 0.00024	0.04408 ± 0.00010	94.046 ± 0.848	1087.091 ± 10.568	0.00183 ± 0.00006	0.9949		
		30.53	101.32	9.2	2.27	2.09	10.44 ± 0.30	0.01007 ± 0.00020	0.01381 ± 0.00022	0.02601 ± 0.00012	166.039 ± 4.074	1656.997 ± 14.788	0.00056 ± 0.00004	0.9893		
		101.32	305.24	10.2	2.09	2.03	10.20 ± 0.32	0.00031 ± 0.00008	0.01731 ± 0.00048	0.00012 ± 0.00008	363.677 ± 15.608		0.00002 ± 0.00076	0.9485	Stick-slip, Single b, Dc	
		305.24	1021.20	9.2	2.03	1.87	10.66 ± 0.30	0.01128 ± 0.00001	0.02430 ± 0.00001	0.02546 ± 0.00001	14.404 ± 0.001	817.239 ± 0.001	0.00372 ± 0.00001	0.9549	Stick-slip	
u253	Set-C	24.51	118.90	23.7	1.13	1.31	10 ^b	0.00428 ± 0.00014	0.00354 ± 0.00014	0.00001 ± 0.00014	179.881 ± 10.844		0.00001 ± 0.00014	0.8244	Single b, Dc	
		118.90	1071.10	21.5	1.31	1.25	10 ^b	0.0006 ± 0.00006	0.00713 ± 0.00058	0.00361 ± 0.00058	281.793 ± 14.110	721.157 ± 56.650	0.00137 ± 0.00001	0.9923	^c	
		1071.10	10581.40	106.3	1.25	0.92	~0									

^aAvailable velocity ranges for each gear and motor set: set-A (0.001–10 $\mu\text{m/s}$); set-B (0.1–1000 $\mu\text{m/s}$); set-C (10–10000 $\mu\text{m/s}$).

^bBecause the motor velocity output V_{ip} was not available for set-C, values of α were estimated using u243 as a reference.

^cInversion failed to converge or not well-matched.

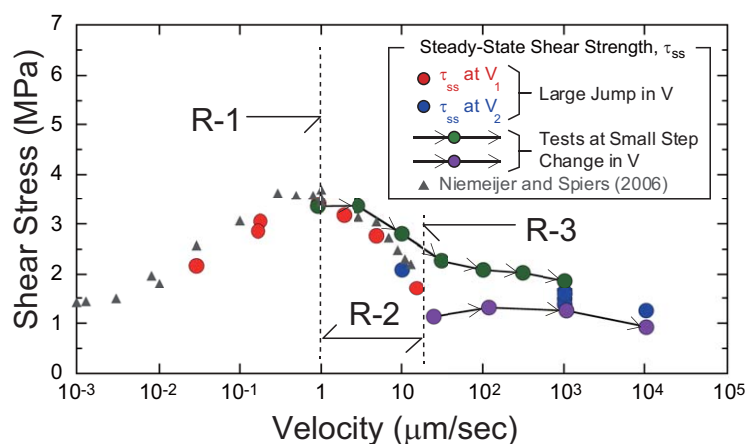


Figure 2. Compilation plot showing the present data on steady state shear strength τ_{ss} as a function of sliding velocity for 80 wt % halite and 20 wt % muscovite gouge mixtures, alongside results of previous work (triangles) [Niemeijer and Spiers, 2006]. The values of τ_{ss} obtained at the velocities V_1 (red circles) and at V_2 (blue circles) constituting the large (multiorder) velocity steps, and in the small (half and 1 order) velocity step sequences (green and purple circles), are the data obtained in the present study. Because of the smaller displacements achieved in the half-order velocity step sequences (green circles), steady state was not attained at all velocities employed in these steps. Three characteristic velocity regimes can be distinguished based on the steady state shear strength: a velocity strengthening regime (R-1: $V \leq 1 \mu\text{m/s}$), a velocity-weakening regime (R-2: $1 \mu\text{m/s} < V \leq 20 \mu\text{m/s}$), and a near velocity-neutral regime (R-3: $V > 20 \mu\text{m/s}$).

Both microstructures reported in that study were uniformly developed, suggesting that deformation was pervasive in the gouge zones.

The microstructures shown here were the result of a sliding history involving two sliding velocities, V_1 and V_2 , imposed after an initial run in with V_0 . We assume that the microstructure developed at V_0 was similar to that presented in Niemeijer and Spiers [2005, Figure 10d], i.e., a porous, chaotic, and cataclastic structure developed at a constant velocity of $13 \mu\text{m/s}$. One purpose of this study was to identify microstructural changes caused by fast slip being imposed on the microstructures developed during the slow, aseismic (velocity strengthening) slip period, i.e., regime R-1 in this study. Figure 6 shows the typical structures obtained at different V_1 (6a–6c: $0.17 \mu\text{m/s}$, i.e., in R-1; 6d and 6e: $0.96 \mu\text{m/s}$, at the boundary between R-1 and R-2; 6f and 6g: $5.00 \mu\text{m/s}$, in R-2), stepping up to a constant $V_2 = 1.02 \text{ mm/s}$. Comparing SEM micrographs of Figure 6a ($V_1 = 0.17 \mu\text{m/s}$) and Figure 6f ($V_1 = 5.00 \mu\text{m/s}$) with micrographs in Figure 10b ($V = 0.1 \mu\text{m/s}$) and Figure 10c ($V = 5 \mu\text{m/s}$) in Niemeijer and Spiers [2005], respectively, we can see reproducibility in the formation of the microstructures. All SEM micrographs display a well-defined shear-localized zone (of thickness $10\text{--}30 \mu\text{m}$) at the boundary (mainly at the rotating piston side), which was not observed by Niemeijer and Spiers [2005]. Figure 6a shows the full gouge layer width with imprints of the piston teeth at both sides, while the gouge layers displayed in Figures 6d and 6f split along a localized boundary shear zone at the rotating piston side (lower), as indicated by the absence of teeth imprints on one side of the sample and the presence of a sharply cleaved boundary instead. However, due to this intense localization, earlier structures, presumably developed at velocity V_1 were still preserved in large parts of the gouge body. We also observed a gradual change in microstructure with increasing V_1 , consisting of a progressive weakening in intensity of the mylonitic fabric, and increasing porosity mainly distributed along bands having a Riedel-1 orientation (Figures 6d and 6f), in agreement with previous studies [Niemeijer and Spiers, 2005, 2006, 2007]. It is believed that pressure solution creep dominates the rate dependence of deformation under velocity-strengthening, mylonitic structure forming conditions (R-1 as shown in Figure 6b) [Bos *et al.*, 2000a, 2000b; Bos and Spiers, 2002]. Although the micrographs of samples deformed in the velocity-weakening regime (R-2) display (a) higher porosities along the Riedel-1 orientations (also along some P-shear orientations as enlarged views in Figures 6d and 6f showed), and (b) more widespread cataclastic microstructures with increasing V_1 , pressure solution creep must also have operated at significant rates up to $V_1 = 5.00 \mu\text{m/s}$, since these samples still contain rounded and sigmoidal halite grains as seen in Figure 6g.

microstructures developed in the gouge zone, with a clear foliation and markedly sigmoidal porphyroclasts. However, in the velocity-weakening regime (R-2) at $1 \mu\text{m/s} < V < 13 \mu\text{m/s}$, a porous, chaotic, and cataclastic microstructure was observed, with equiaxed clasts and no foliation developed. Typical examples of the microstructures observed in the R-1 and R-2 regimes, illustrating this (progressive) weakening in intensity of the mylonitic fabric with increasing the velocity, were published by Niemeijer and Spiers [2005] in Figure 10a ($V = 0.03 \mu\text{m/s}$), Figure 10b ($V = 0.1 \mu\text{m/s}$), Figure 10c ($V = 5 \mu\text{m/s}$), and Figure 10d ($V = 13 \mu\text{m/s}$) of their paper.

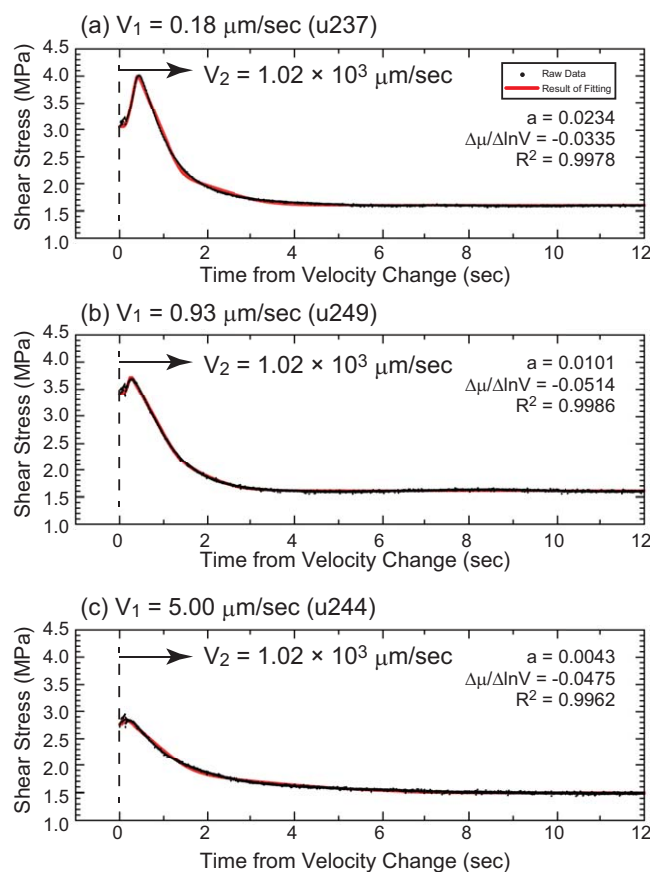


Figure 3. The direct effect and subsequent evolution of shear strength following a change in sliding velocity (black dots) from three different initial velocities V_1 ((a) 0.18 $\mu\text{m/s}$, (b) 0.96 $\mu\text{m/s}$, and (c) 5.00 $\mu\text{m/s}$) to a constant velocity $V_2 = 1.02 \text{ mm/s}$. The steady state shear strength at V_2 is almost constant at 1.5–1.6 MPa and is V_1 -independent. Note that the direct effect a , decreases in magnitude as V_1 increases in Figures 3a–3c. Red lines show results of curve fitting using RSF law.

The well-defined shear localization band at the boundary of the gouge layer presumably corresponds to a zone of high-strain-rate deformation at V_2 . This hypothesis is supported by the previous study showing the microscopic observations resulted from hold-slide-hold, multistep tests [Niemeijer and Spiers, 2006, Figures 9 and 10], indicating relatively homogeneous deformation structures without a shear localization at the boundary under both velocity conditions of R-1 and R-2 regimes. A product of u242 (Figure 7) deformed at $V_1 = 0.03 \mu\text{m/s}$ (within the velocity-strengthening regime, R-1) and $V_2 = 10.17 \mu\text{m/s}$ (close to upper limit in velocity of the velocity-weakening regime, R-2) showed a similar structure with those shown in both u238 (Figures 6a) and Figure 10a ($V = 0.03 \mu\text{m/s}$) in Niemeijer and Spiers [2005]. A well-developed mylonitic structure (Figure 7b) was intersected by a thin and well-defined localized zone (ca. 10 μm in thickness in SEM observation) at both sides of the boundaries (Figures 7a, 7c, and 7d), but was not overprinted by the porous, chaotic, and cataclastic structures that correspond to the high-velocity regime at $V = 13 \mu\text{m/s}$ as observed in Niemeijer and Spiers [2005, Figure 10d]. Localization could be recognized at the boundary between the main gouge and gouge stuck in

grooves of the piston teeth (Figure 1), defined by almost continuous planes of comminuted and aligned muscovite phyllae (such as Figures 6c and 7c) surrounding severely comminuted halite grains with $\sim 1 \mu\text{m}$ in grain size (see Figures 6e, 7c, and 7d).

We also performed a higher-velocity experiment, u239 (Figure 8), where V_1 and V_2 were 15.32 $\mu\text{m/s}$ (almost upper limit in velocity of the velocity-weakening regime, R-2) and 1.05 cm/s (within the velocity-neutral regime, R-3) respectively, resulting in a highly porous random structure of angular halite grains (Figure 8a) combined with intense shear localization at the rotation side boundary (Figure 8b). The grains in the main body of the gouge have fewer contacts with each other than cases deformed at lower V_1 (Figures 6 and 7). Because of the lack of cohesion of the experimental product of u239, the thin section has many large pores which might be an artifact from sample preparation. Nonetheless, a comminuted localized zone was also identified at the rotation side boundary. The porous body of the bulk gouge zone could possibly have formed at V_1 , as shown in previous result at Figure 10d ($V = 13 \mu\text{m/s}$) by Niemeijer and Spiers [2005]. However, it might be difficult to conclude that high-velocity shear at V_2 has been imposed only in the comminuted localized zone. As continuous dilation occurred during shearing at both V_1 and V_2 , axial strain (dilation measured positive) increased toward 17.5% during high-velocity sliding, relative to the thickness at the start of the velocity step (0.935 mm). It seems unlikely that the dilation concentrates in 50 μm thick localized zone as recognized in Figure 8b, since this would correspond to an unrealistically large axial strain (328%) at the localized zone. The 17.5% dilation in the body of the gouge next to the localized zone of comminution might occur after stepping to highest velocity of V_2 , because the body of the gouge was initially incohesive and deformed via

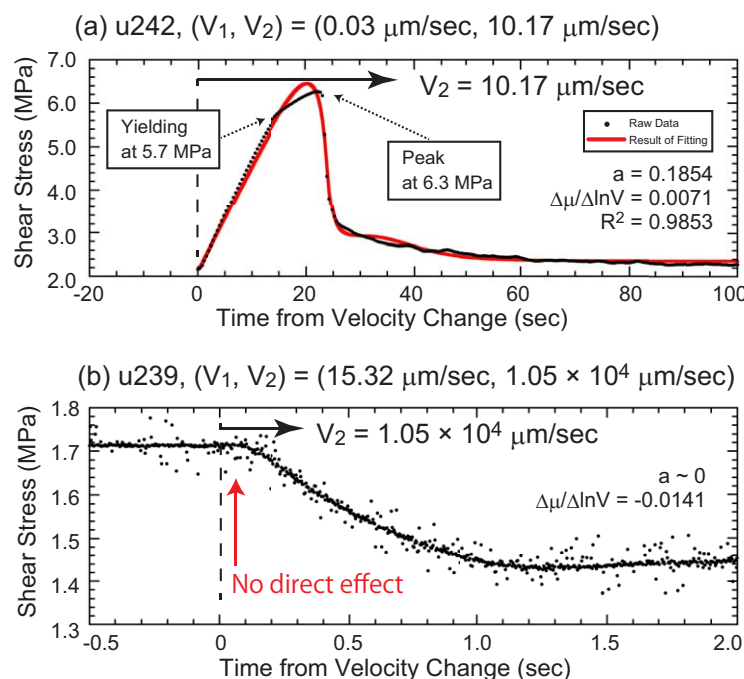


Figure 4. The direct effect and subsequent evolution of shear strength following a change in sliding velocity (black dots) for two cases. (a) u242: the lowest pair of velocities. Here an abnormally large direct effect is obtained in stepping from $V_1 = 0.03 \mu\text{m/s}$ to $V_2 = 10.17 \mu\text{m/s}$, but the RSF model (red line, the best fit curve) does not well explain the evolution behavior. (b) u239: the highest pair of velocities. Here no direct effect is observed in stepping from $V_1 = 15.32 \mu\text{m/s}$ to $V_2 = 1.05 \text{ cm/s}$.

neous response and following transient behavior of samples u237 (Figure 3a) and u238 (Figure A1a) were very different from that of u242 (Figure 4a). Although all of these experiments developed a well-matured mylonitic microstructure (Figures 6a, 6b, and 7), the direct effect measured in u242, having a velocity jump of almost 2.5 orders of magnitude from $V_1 = 0.03 \mu\text{m/s}$ to $V_2 = 10.17 \mu\text{m/s}$, was significantly larger than that measured in u237 and u238 (almost 3.7 orders of magnitude jump from $V_1 = 0.2 \mu\text{m/s}$ to $V_2 = 1 \text{ mm/s}$). The difference in the direct effect would be controlled by the up-step velocity, exceeding $20 \mu\text{m/s}$ in the case of u237 and u238 but not in u242. In the next section, we will discuss possible causes for the significant difference in the transient behavior. In this discussion, we will explicate the importance of the critical velocity V_c ($\sim 20 \mu\text{m/s}$) corresponding to the velocity marking the transition from the R-2 to the R-3 regime.

4. Discussion

4.1. Velocity-Dependent Steady State Frictional Strength

It was found that the steady state shear strength at a given velocity was not sensitive to the velocity history (Figure 2). From our data of the steady state shear strength, we defined three regimes of frictional behavior: a velocity-strengthening regime at low velocities (R-1, $V < 1 \mu\text{m/s}$), a velocity-weakening regime at intermediate velocities (R-2, $1 < V < 20 \mu\text{m/s}$), and a velocity-neutral regime at the highest velocities (R-3, $V > 20 \mu\text{m/s}$). The velocity-neutral regime at R-3 has been predicted by *Niemeijer and Spiers* [2007], but was not found experimentally by these authors.

At the highest velocities (both V_1 and $V_2 > V_c$), we found that the shear strength remains constant at around 1–1.5 MPa (corresponding μ of 0.2–0.3; Figure 5a). This observation is consistent with the conceptual model of *Niemeijer and Spiers* [2007], which states that the macroscopic friction coefficient at high velocities approaches that of the muscovite foliation. In their model, shear strain is accommodated by granular flow of halite grains, facilitated by a low friction, intergranular muscovite matrix, and it is assumed that, at steady-state, the pressure solution compaction rate is balanced by the dilatation rate resulting from granular flow. After an increase in sliding velocity, the system dilates toward a new steady state porosity, and

granular flow. However, to confidently answer the question of which deformation feature, dilation or shear localization, was dominant in the R-3 regime requires further study.

We observed localization features in the form of boundary shear bands in all experiments with large steps in velocity, independently of the initial velocity and thus independent of the initial gouge microstructure. These localized shear bands were narrow in thickness (10–50 μm) and sharply cross-cut the bulk of the gouge without completely overprinting the initial microstructure, a feature that is not only found in high-speed shear experiments [e.g., *Smith et al.*, 2015, 2016], but also in natural carbonate faults [e.g., *Smith et al.*, 2011; *Demurtas et al.*, 2016]. The instanta-

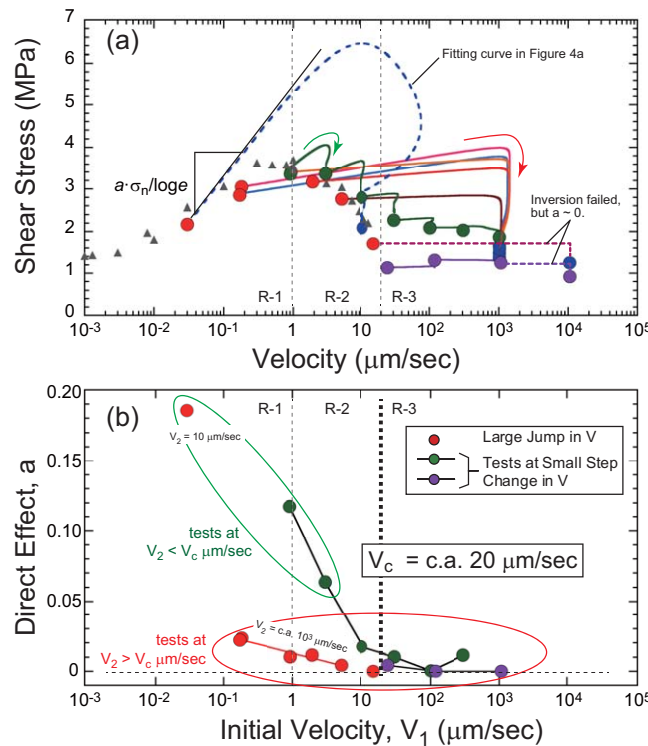


Figure 5. (a) Compilation of shear strength evolution with velocity *V* for every velocity step change test, using the results of nonlinear least square curve fitting (see Appendix A). The initially linear shear strength-increment per increment of log(*V*) is proportional to the direct effect *a*. (b) The direct effect, as a function of the velocity before the step change, *V*₁. We found (1) a decreasing magnitude of *a* with increasing *V*₁, and (2) a large difference in *a*, depending on whether *V*₂ crossed over *V*_c (ca. 20 μm/s) (red ellipses) or not (green ellipses). Errors (2SD) were much smaller in size than the size of the markers (see Table 1). Legends are the same as in Figure 2.

close to φ_c . Moreover, SEM micrographs of the localized zones (Figures 6c, 6e, 7c, 7d, and 8b) show that the muscovite folia aligned along Riedel-Y shear planes consisting of 10–50 μm thick layers of comminuted halite grains. This supports the model of Niemeijer and Spiers [2007] that the frictional strength at high velocity, meaning at near critical state, is controlled by frictional sliding between the muscovite folia alignment and halite alignment along Riedel-Y shear planes. At the same time, slip at the critical state characterizing velocity-neutral behavior on the phyllosilicates would minimize the average grain contact area (and hence, from equation (2), lead to constant shear strength).

4.2. Velocity-Dependent Direct Effect

We observed drastic changes in the behavior of the direct effect when the velocity was changed across the regimes of different dominating mechanisms (Figure 5b). It was found that the steady state shear strength was not sensitive to the velocity history (Figure 2). However, the direct effect *a* was found to decrease with increasing *V*₁ and/or *V*₂. Additionally, the direct effect for velocity steps reaching *V*₂ values beyond a critical velocity of around 20 μm/s, i.e. steps crossing the boundary between the velocity-weakening regime (R-2) and the velocity-neutral regime (R-3), was very different from that produced by smaller velocity steps (Figure 5). A critical velocity (*V*_c ~ 20 μm/s), corresponding to the boundary between the velocity-weakening regime (R-2) and the velocity-neutral regime (R-3), can be also defined by the disappearance of the direct effect (Figure 5b). Moreover, the direct effect at sets of the lower velocity of both *V*₁ (in R-1) and *V*₂ (not exceeding R-2) resulted in abnormally large values for the direct effect, exceeding values of 0.1 (Figure 5b). Typically, values of the direct effect, obtained from many experiments using a velocity step change technique for noncoherent powdered rock materials at conditions where frictional behavior dominates the overall rheology, are of the order of or smaller than 0.01 [e.g., Blanpied et al., 1998; Reinen et al., 1994; Ikari et al.,

from a force balance at the microscale it follows that the shear strength reduces, hence velocity-weakening behavior is produced. The relationship between the porosity-dependent dilatancy angle ψ and shear strength was expressed as

$$\tau = A_G \left(\frac{\tan \psi}{\cos \psi - \mu_{h-m} \cdot \sin \psi} \right) \cdot S_{coh} + \left(\frac{\sin \psi + \mu_{h-m} \cdot \cos \psi}{\cos \psi - \mu_{h-m} \cdot \sin \psi} \right) \cdot \sigma_n, \quad (2)$$

where *A*_G is a geometrical factor, *S*_{coh} is a cohesion of grain contacts, and μ_{h-m} is friction coefficient within the muscovite folia at the halite contacts [Niemeijer and Spiers, 2007]. The dilatancy angle ($\psi \geq 0$) was expressed as a function of porosity φ . As shown by Niemeijer and Spiers [2007], this means that ψ is a function of a ratio of the real contact area to the apparent area, *R*, as

$$R = A_G \tan \psi. \quad (3)$$

At the critical state, i.e., $\psi = 0$ in equation (2) when φ converges to the critical state porosity φ_c , τ/σ_n approaches the value of μ_{h-m} (ca. 0.3 in Niemeijer and Spiers [2007]). Therefore, since we observe velocity-neutral behavior at R-3, it can be hypothesized that the porosity in the localized zone is at or

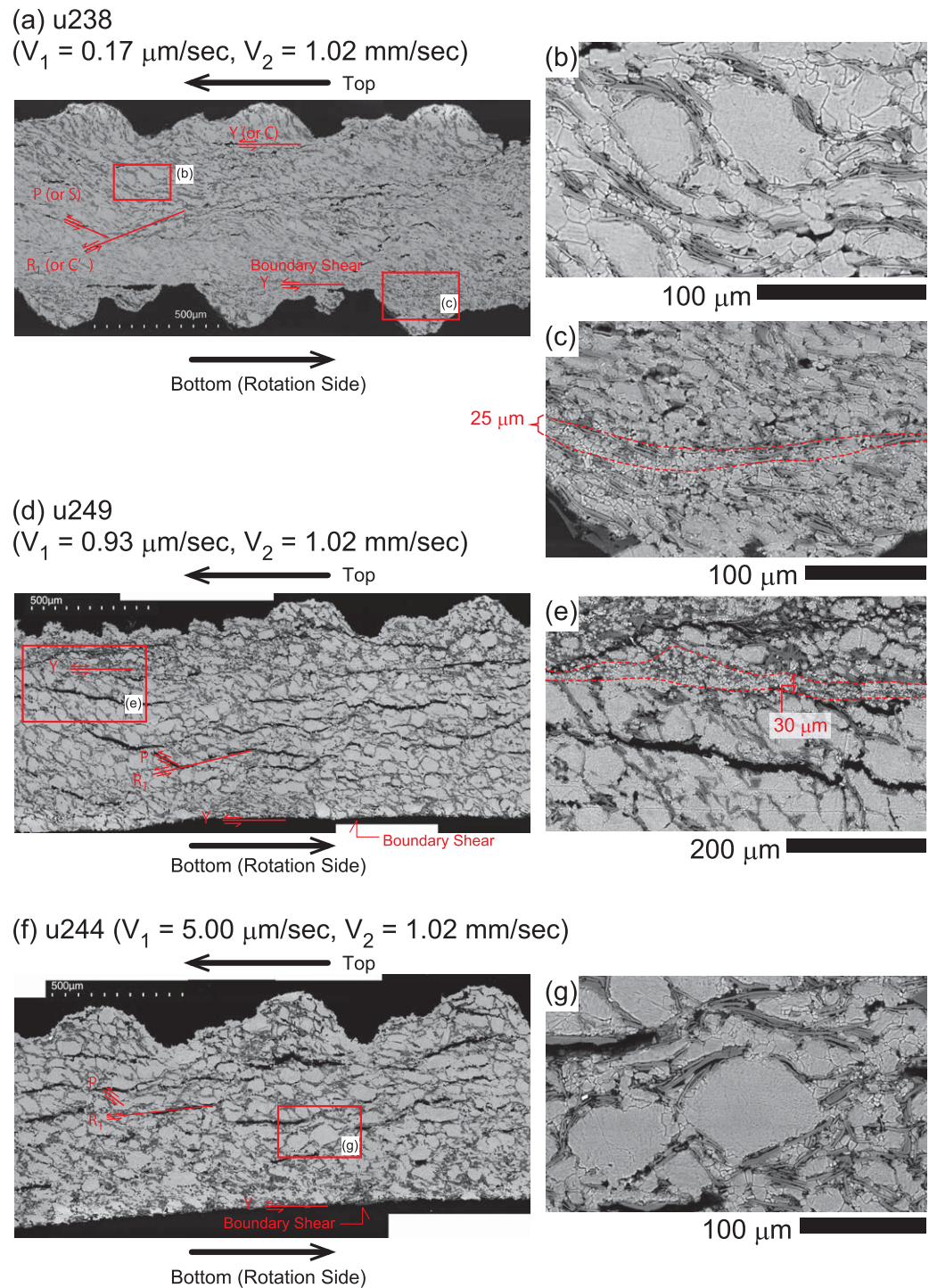


Figure 6. SEM microphotograph of samples deformed at different V_1 . (a–c) u238; $V_1 = 0.17 \mu\text{m/s}$, (d, e) u249; $V_1 = 0.93 \mu\text{m/s}$ at (f, g) u244; $V_1 = 5.00 \mu\text{m/s}$, but with constant $V_2 = 1.02 \text{ mm/s}$. Arrows indicate the shear sense. The bottom of the microphotographs is the rotating side. With increasing V_1 , the mylonitic structure such as (b) became less well developed and porosity increases notably along the Riedel shears (d, f), see red arrows (R1 and P shears, mainly). Localization could be recognized as a discontinuity to cut the preformed structure at the boundary between main gouge layer and the gouge stuck in grooves of the piston teeth, defined by almost continuous planes of comminuted halite and aligned muscovite folia, such as Figures 6c and 6e. (g) Rounded and sigmoidal halite grains at relatively high V_1 (u244; $5.00 \mu\text{m/s}$) was an evidence that pressure solution creep must also have operated at significant rates.

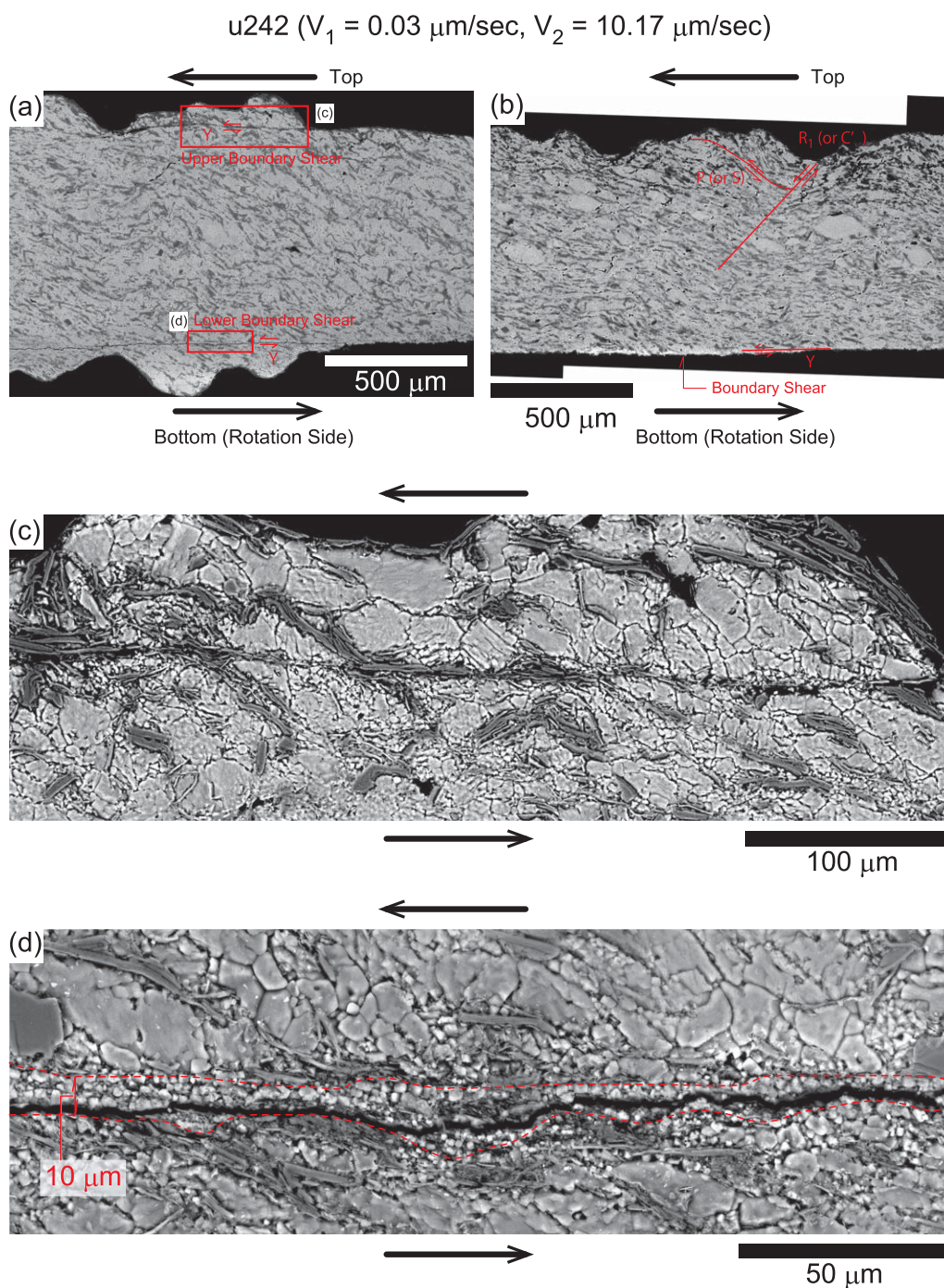


Figure 7. SEM micrographs of the product of experiment u242, deformed at $(V_1, V_2) = (0.03, 10.17 \mu\text{m/s})$. Arrows indicate the shear sense. (a) Wide view of the product shows that the mylonitic structure produced by pressure solution creep at low velocity V_1 was cut by a sharp discontinuity cutting the mylonitic structure at both sides of the boundary. (b) Another wide view of the most matured mylonitic structure obtained in the experiments, characterized by sigmoidal halite grains surrounded by sigmoidal foliation. At the bottom of the specimen (rotating side) the sample has split at the interface of a boundary shear caused by shear localization at the velocity V_2 . Enlarged SEM views of (a) centered at a narrow zone of shear localization (c, top; d, bottom). Localization was characterized by several slip planes of comminuted muscovite which aligned along comminuted halite grains.

2009; Takahashi et al., 2011]. Bos and Spiers [2002] have roughly estimated values of the direct effect for brine-saturated monomineral halite gouge at $\sigma_n = 2.5 \text{ MPa}$, which were found to be abnormally high, ranging from 0.17 to 0.40. The abnormally large direct effect of more than 0.1, thus, would reflect the time-

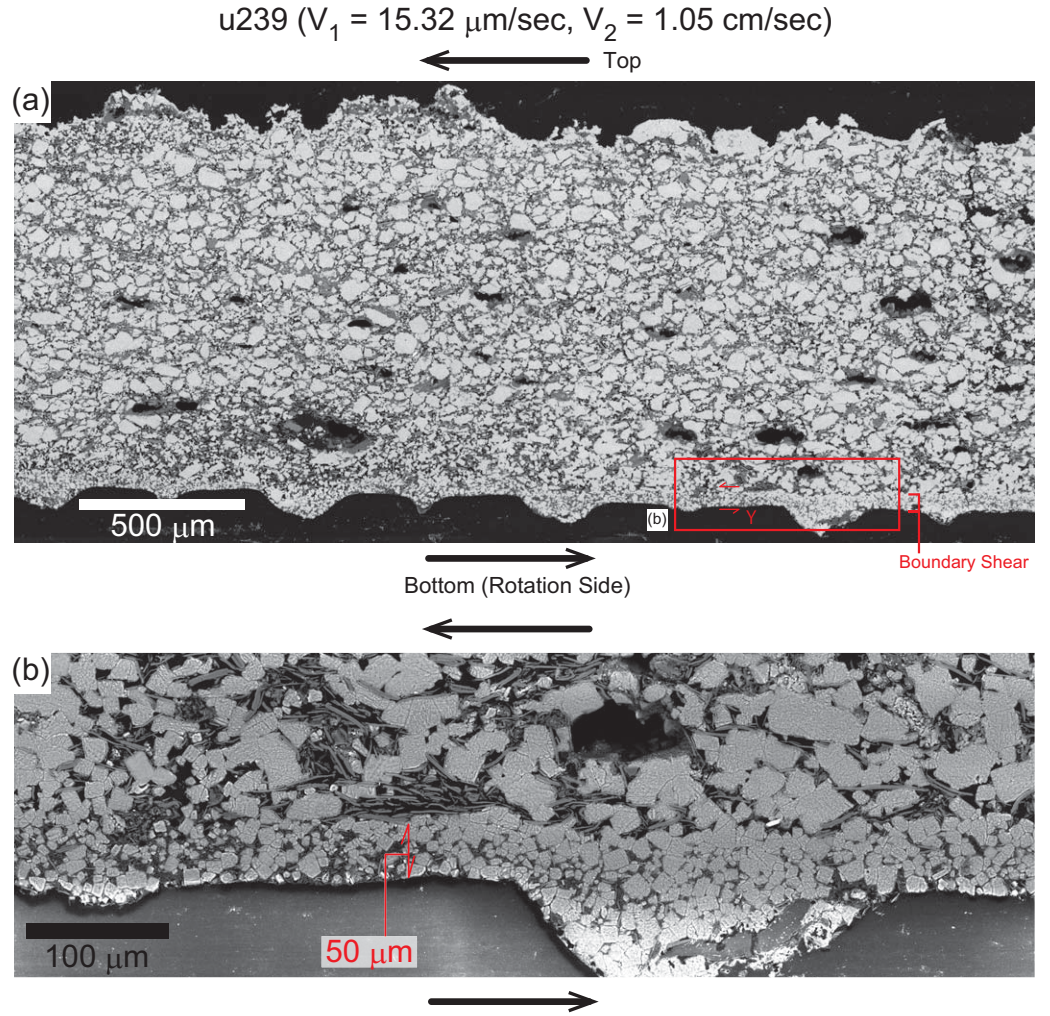


Figure 8. (a) Wide view SEM micrograph of the product of experiment u239, deformed at $(V_1, V_2) = (15.32 \mu\text{m/sec}, 1.05 \text{ cm/s})$. Black arrows indicate shear sense. The black spots in the specimen are holes that developed during section preparation of the highly incohesive and porous gouge with angular halite grains. (b) Note the finely comminuted localized zone of around $50 \mu\text{m}$ in thickness at the bottom face of the sample (rotation side).

dependent compaction property of halite under the condition where pressure solution creep was proceeding [Bos and Spiers, 2002; Niemeijer and Spiers, 2006].

It has been proposed that the direct effect can be expressed as a thermally activated process at the grain contacts (herein a_T), as follows:

$$a_T = \frac{k_B T}{P \Omega}, \quad (4)$$

where P is interpreted as a hardness or yield strength of asperity contacts, Ω is the activation volume, k_B the Boltzmann constant, and T the absolute temperature [Brecht and Estrin, 1994; Nakatani, 2001]. Here P is equal to σ_n/R and is regarded as a constant because of a linear relationship between σ_n and R for a single slip surface case [e.g., Logan and Teufel, 1986]. However, to be more accurate, P is $\sigma_n/R(V_1)$ where $R(V_1)$ is a ratio of steady state real contact area to the apparent area at V_1 (introduced from Hatano [2015]; detailed explanation in section A2), and it then follows that

$$a = \frac{k_B T}{\Omega} \cdot \frac{R(V_1)}{\sigma_n}. \quad (5)$$

For gouges deforming at higher velocity ($>1 \mu\text{m/s}$) where the dilation controls the shear stress, it is expected that R is a function of ψ shown as (3), which in turn depends on V . Therefore, P can no longer be

assumed to be constant with changing V . Substitution of equation (3) into (5) gives a relationship between the direct effect and the dilatation angle ψ , for the velocity-weakening and neutral regimes (R-2 and R-3), as

$$a = \frac{k_B T}{\Omega} \cdot \frac{A_G \tan \psi(V_1)}{\sigma_n}. \quad (6)$$

The observation that a is inversely related to V_1 ($V_1 < V_c$) implies a decrease in the real contact area ratio, R , with increasing V_1 , as expressed in equation (5). The microstructural observation and results of porosity measurements by *Niemeijer and Spiers* [2006] under the same experimental conditions show that the porosity in the gouges increases with increasing V_1 . Our experiments support these observations (Figures 6–8). The direct effect decreases toward zero when both V_1 and V_2 are larger than V_c , possibly indicating that the change in real contact area approaches zero, i.e., the real contact area is minimized. At the highest velocities (both V_1 and $V_2 > V_c$), Figure 5a displays that the shear strength remains nearly constant at around 1–1.5 MPa (corresponding μ of 0.2–0.3). Such low friction is facilitated by cohesionless granular flow of the gouge and slip on the muscovite folia [*Niemeijer and Spiers*, 2007]. On the other hand in the velocity-strengthening regime (R-1, $V < 1 \mu\text{m/s}$), the real contact area increase is predominantly offered by the time-dependent pressure solution creep. We suppose that $R(V_1)$ would also strongly contribute to the direct effect for R-1 regime, except that a feature of velocity dependent direct effect may be different from equation (6). However, in the experiment u242 we could not determine an accurate value of the direct effect (Figure 4a). The instantaneous strengthening at almost 2.5 orders of magnitude increase in V from a steady state shear strength at $V_1 = 0.03 \mu\text{m/s}$ may be larger than the yielding stress (5.7 MPa) of the cohesive mylonitic gouge reworked at $V_2 = 10.17 \mu\text{m/s}$.

A question that remains to be addressed is that of the history dependence of the direct effect. Even if V_1 fell in R-1 (as seen in Figure 5b, red circles), the direct effect was found to be significantly smaller for large velocity steps toward $V_2 (> V_c)$, than for small velocity steps (green circles). Equation (5) implies that the direct effect depends on V_1 but not on V_2 , assuming a constant activation volume Ω . Equation (5) was derived under the assumption that the changes in velocity are mathematically instantaneous and infinitesimally small, with accordingly no change in the strength of the sliding interface during acceleration and elastic loading. However, when a large step in velocity is imposed, the direct effect is likely to be affected by microstructural evolution reducing the strength of the sliding interface during acceleration toward V_2 . In addition to this strength reduction of the sliding interface, the style of deformation could have switched from pervasive at low velocities, to localized in a narrow shear band at high velocities producing higher internal shear strain rates and larger strain.

Another topic that we did not touch upon here is to try to describe the evolution effect b , associated with a characteristic displacement D_c . We found that the steady state shear strength τ_{ss} is independent of the velocity history (Figure 2), but the direct effect a depends on both V_1 and V_2 . Although the steady state shear strength τ_{ss} demonstrated robust three regimes of velocity dependence (velocity-strengthening, weakening, and neutral), an inclination to unstable sliding of the fault, meaning the magnitude and sign of $(b-a)/D_c$ should be determined by a combination of (V_1, V_2) for the cases that the poststep velocity crosses a boundary or boundaries of the velocity regimes. The evolution effect seemed to play a role to provide a balance between a and $\Delta\tau_{ss}/\ln(V_2/V_1)$. In other words, the evolution behavior may be linked such that the steady state shear strength always evolves toward a predefined value, regardless of the magnitude of the direct effect. However, we reserve it for future studies to specifically describe b and D_c as a function of both V_1 and V_2 .

4.3. Deformation Mode Switching From Distributed to Localized in Mylonitic Rock

Micrographs from a previous study [*Niemeijer and Spiers*, 2005, Figure 10] displayed no sharp shear-localized zones at the boundary of the gouge body for both samples deformed at 0.03 and 13 $\mu\text{m/s}$. This supports the idea that the sharp localization in our samples probably formed after the velocity step (Figures 6 and 7) and that the mode of deformation switched from one producing pervasive mylonitic structures to one of slip on brittle localized shear bands at $V > V_c$.

The specimen developing a mylonitic structure (composite planar fabric such as S-C and -C' structures) at low velocities was characterized by low strength ($\mu \sim 0.3$), as was the specimen sheared under high-velocity conditions (Figure 2). However, the mylonitic structure is more cohesive than the cataclastic structure developed at high velocity. Pervasive pressure solution creep of the salt clasts at low velocity reduces the sample

porosity and allows for extremely large real contact area at contacts of halite-halite grains and halite-muscovite folia. Once the “cohesive” mylonitic structure is formed, it may be energetically unfavorable to dilate and destroy the mylonitic structure completely, even after the velocity increases. Instead, deformation at high velocity tends to concentrate in a weak boundary zone, forming a new shear band as found in the observed boundary shear bands measuring 10–30 μm in thickness (Figures 6c, 6e, 7c, and 7d). Because of the increased porosity at the boundary shear zone as compared to the bulk, and the contrast in material strength and stiffness, stresses are intensified at the tips of the teeth in the steel rings (Figure 1). Moreover, because of the velocity-weakening nature of the gouge material at high velocities or shear strain rates, deformation will tend to localize further at the weakest zone [Beeler *et al.*, 1996]. Additionally, dilatancy will then occur in the narrow boundary shear zone with the internal porosity of the shear band increasing toward φ_c for velocities $>V_c$, resulting in the velocity-neutral dependence of the frictional strength (R-3).

The microstructural evolution described above explains why an abnormally large direct effect of $a = 0.19$ was observed in experiment u242 with $(V_1, V_2) = (0.03, 10.17 \mu\text{m/s})$. That abnormally large value of the direct effect was almost equal to the value for 100% halite gouge (estimated from Bos and Spiers [2002]). This increase in the direct effect can be attributed to a substantial increase in the real contact area due to pressure solution creep of halite while sliding at $V_1 = 0.03 \mu\text{m/s}$, as it is expected that the direct effect is proportional to the real contact area (5). We speculate that the anomalously high strength (6.3 MPa) at the peak of the instantaneous response of u242 (Figure 4a) reflects a response to preserve the extremely large contact area at $V_2 = 10.17 \mu\text{m/s}$ on the cohesive mylonitic structured gouge. However, its steady state strength (τ_{ss}) at $V_2 = 10.17 \mu\text{m/s}$ was substantially lower (1.5 MPa). Hence, we believe that the deformation mode switched from distributed to localized in a narrow, brittle fracture. Furthermore, the transient behavior exhibited by u242 more closely resembled the behavior of a triaxial failure-test with a distinct yield point, peak-stress and rapid stress drop [Paterson, 1978; Lama and Vutukuri, 1978], or constant velocity and slide-hold-slide tests such as those by Smith *et al.* [2015] and Van den Ende *et al.* [2016], rather than the behavior typically observed in velocity-step tests (see Figure 4a). The behavior that we observed evokes the hypothesis that the mylonitic gouge developed over long periods, due to pressure solution creep, acquires a much higher strength than the measured peak stress at $V_2 = 10.17 \mu\text{m/s}$, since the gouge structure at $V_1 = 0.03 \mu\text{m/s}$ is very dense (large contact area) and cohesive (Figure 7). Thus, the shear stress required to completely rework this mylonitic structure in a distributed fashion at $V_2 = 10.17 \mu\text{m/s}$ is higher than the stress required to form a new fracture (localization on a boundary shear). Additionally, the estimated overshoot in velocity (up to 80 $\mu\text{m/s}$; Figure 5a) is larger than V_c and so it is likely that the intense localization was developed during the overshoot, while preserving the original mylonitic structure. On the other hand, at both V_1 and $V_2 > V_c$ the direct effect vanishes because the dilatancy angle ψ in the shear zone approaches zero. Between these two extreme cases, cases at $V_1 < V_c < V_2$ produced intermediate (but small) values of the direct effect. Based on these observations, our hypothesis is that structural development toward localization from pervasive distribution of shear would be a quickly evolving phenomenon during acceleration of slip, resulting in smaller instantaneous resistance, when the velocity exceeds the critical velocity V_c . In this study, we also did not touch upon a role of finite strain for the deformation mode switching to localization. In nature, the fault acceleration associated with the strain localization would be a spontaneous strain concentrating phenomenon to weaken the fault at the earthquake nucleation stage. Future experimental study requires the investigation of the microstructural development with variable slip pulses, perhaps under shear stress controlled boundary conditions.

4.4. Presence of a Critical Velocity for the Absence of a Direct Effect

This study provides several new and important perspectives for earthquake nucleation and propagation processes. It has been found in numerical studies of earthquake nucleation that not only the magnitude of $(a-b)$, but also the ratio of a/b of the seismogenic patch affects the behavior of the fault. Specifically, the nucleation size increases with, and preseismic slip is promoted by, an increase in a/b [Rubin and Ampuero, 2005; Noda and Hori, 2014]. The positive direct effect is very important to allow the existence of a low-velocity slip range that can be regarded as “quasi-static,” which has a role to stabilize the fault slip response caused by perturbation in the velocity at low enough slip rate. Here the quasi-static velocity V_{q-s} satisfies the condition $V_{q-s} \ll 2a\sigma_n V_s/G$ where V_s is the S wave velocity and G is the shear modulus of the faulted medium [Rice *et al.*, 2001]. If $a = 0$, faults responding to any small perturbations will behave “dynamically” at all higher velocities. Therefore, variations in the direct effect may affect the characteristics and evolution of the seismogenic patch. From our observations, it is apparent that the direct effect strongly diminishes when the velocity exceeds the critical velocity V_c (Figure 5). Thus, independently of the velocity history, once the velocity exceeds V_c , acceleration toward

“runaway slip” no longer requires relatively slowly accelerating preseismic slip at the end of the earthquake nucleation stage, since $a/b \sim 0$ at $V > V_c$. Additionally, we propose that the style of deformation changes from pervasive/distributed to localized when the critical velocity is exceeded. In order to understand the process of earthquake nucleation and propagation better and to improve models of the seismic cycle, it is important to obtain a measure of the value of V_c in natural faults, as this velocity marks the boundary beyond which the initial resistance to slip acceleration is greatly reduced. Additional experiments should be conducted to thoroughly test our hypotheses. Since earthquake nucleation and propagation is a natural and spontaneous process, investigating the role played by localization occurring within a mylonitic rock is one of the next targets of our research.

5. Conclusions

The aim of this study was to investigate shear localization in simulated fault gouges exhibiting a preexisting mylonitic structure formed at quasi-static strain rates. We performed rotary shear experiments on a brine-saturated simulated gouge, consisting of 80 wt % halite and 20 wt % muscovite, showing various deformation structures associated with two main deformation mechanisms, pressure solution creep and granular flow. At a constant normal stress of 5 MPa and room-temperature conditions, the balance between these mechanisms is dictated by the imposed sliding velocity [Niemeijer and Spiers, 2005, 2006, 2007]. We performed large step-wise increases in sliding velocity from V_1 to V_2 over a wide range of velocities (0.03 $\mu\text{m/s}$ –1.05 cm/s), employing step sizes of several orders of magnitude (up to 2.5–3.5 orders). These velocity steps were imposed after developing a mature mylonitic structure within the gouge, formed at low sliding velocity, to simulate the transient behavior associated with slip acceleration.

Independently of the deformation history of the sample, the steady state shear strength was in good agreement with the previous studies [Niemeijer and Spiers, 2006, 2007], and displayed three main velocity-dependent regimes of the shear strength: a velocity-strengthening regime at low velocities (R-1, $V < 1 \mu\text{m/s}$), a velocity-weakening regime at intermediate velocities (R-2, $1 < V < 20 \mu\text{m/s}$), and a velocity-neutral regime at the highest velocities (R-3, $V > 20 \mu\text{m/s}$). The magnitude of the direct effect a depends strongly on the velocity history. It is significantly smaller when the poststep velocity is larger than a critical velocity, $V_c \sim 20 \mu\text{m/s}$. Since the steady state shear strength does not depend on velocity history, this implies that the evolution effect b is only a dependent variable. Mylonitic microstructures formed at low velocity (R-1) survive shearing at higher velocity in R-2 or R-3, because deformation becomes localized in boundary shears with a ~ 10 – $50 \mu\text{m}$ thick band.

The switch from distributed to localized deformation seems to be controlled by the velocity history and controls the size of the direct effect. The presence of the critical velocity V_c above which the direct effect disappears implies that earthquakes can easily accelerate without the occurrence of preseismic slip. Additional experiments should therefore be conducted at various combinations of sliding velocities V_1 and V_2 , relating to the critical velocity V_c . Moreover, experimental investigations of the presence of the critical velocity V_c should be extended to real fault rock compositions at seismogenic zone P-T conditions.

Appendix A

A1. Method of Obtaining the Parameters in the RSF Law

We determined the frictional parameters and the shear strength versus velocity changes characterizing our velocity stepping experiments, using a nonlinear least square curve fitting technique [Noda and Shimamoto, 2009; Takahashi et al., 2011]. Large jumps in sliding velocity required 0.5 s of acceleration to increase the velocity to V_2 , causing a gradual increase in the shear stress (see Figure A1a for typical data and a result of the analysis). All velocity curves we obtained from data on motor velocity show similar features to that drawn in Figure A1a. We estimated and created a model of an ordinary differential equation (ODE) for load-point velocity V_{lp} using motor velocity data (Figure A1b) and obtained a parameter α in equation (A1).

$$\dot{V}_{lp} = \alpha \cdot V_{lp} \cdot \ln \left(\frac{V_2}{V_{lp}} \right). \quad (\text{A1})$$

The frictional parameters (a , b , and D_c) and the evolution of τ and velocity at gouge zone V_g were obtained by simultaneously solving the ODEs corresponding to equation (A1) and RSF law (1) written in the forms

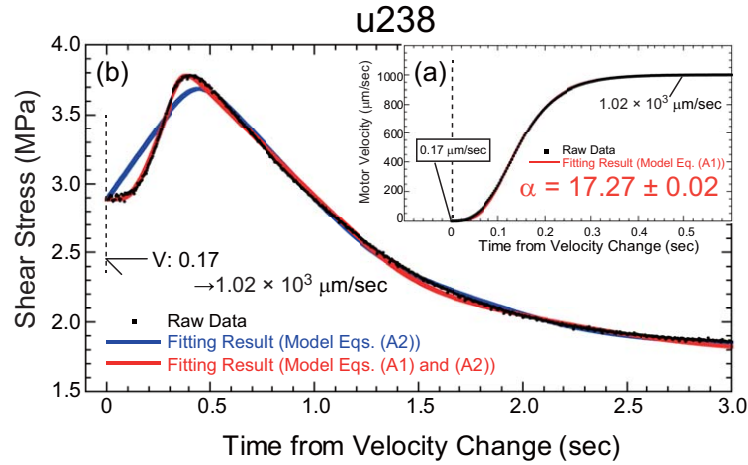


Figure A1. (a) Data of motor velocity (black dots) at the velocity step change from 0.17 $\mu\text{m/s}$ to 1.02 mm/s in experiment u238, plus a fit to the data (red line) made using the model for load-point velocity evolution given in equation (A1). (b) Results of the best fit of RSF behavior, modeled using equation (A2) only (blue line), and using both (A1) and (A2) combined (red line), compared with the raw data (black dots).

$$\Delta\dot{\mu} = \frac{\Delta\dot{\tau}}{\sigma_n} = k(V_{lp} - V_g),$$

$$\dot{V}_g = \frac{V_g}{a} (\Delta\dot{\mu} - b_i \frac{\dot{\theta}_i}{\theta_i}), \quad (\text{A2})$$

with

$\dot{\theta}_i = 1 - \frac{V_g \theta_i}{D_{ci}}$ (aging law [Dieterich, 1979]), where $\Delta\mu$ is the change of the coefficient of friction (defined as τ/σ_n) from the initial state μ_0 , k is the normalized stiffness, and θ_i is the state variable (aging law) ($i = 1, 2$). The initial conditions of $(\Delta\mu, V_{lp}, V_g, \theta_i)$ were $(0, V_1, V_1, D_{ci}/V_1)$. Our analyses include the effect of finite acceleration of V_{lp} , which resulted in a much better model fit at the onset of the response to the large jump, producing more accurate values of the RSF parameters and the trace of τ to V in Figure 3a.

A2. Derivation of the Direct Effect (Caused by the Thermally Activation Process)

Hatano [2015] tried to derive the RSF law (1) by considering atomistic processes at asperities. We simplified his theory in order to explain why the direct effect (caused by the thermally activation process) a_T should be related to the velocity before the step-change, thus V_1 , if other conditions are constant. Hatano [2015] considered not only change in real contact area but also change in areal density of the covalent bonds at an asperity during the state-evolution. Here we neglected an effect of the covalent bonds since this minor difference is not important for this discussion.

The macroscopic shear force F is written by the summation of shear stress τ_i applied to each asperity with an area A_i in an apparent contacting area A_{app}

$$F = \sum_i \tau_i A_i \approx \tau_c A_{real}. \quad (\text{A3})$$

Here τ_c is the representative shear stress on the asperity and A_{real} is the real contact area meaning the summation of each area of the asperities, respectively. When we increase the velocity with a step ΔV ($V_2 = V_1 + \Delta V$), equation (A3) can be rewritten as

$$F(V_2) = F(V_1) + \Delta F = (\tau_c(V_1) + \Delta\tau_c)(A_{real}(V_1) + \Delta A_{real}). \quad (\text{A4})$$

Using that $\Delta\tau_c \Delta A_{real} \sim 0$ and $F(V_1) = \tau_c(V_1) A_{real}(V_1)$, the difference in the friction coefficient $\Delta\mu$ caused by the change in the velocity is

$$\Delta\mu = \frac{\Delta\tau_c A_{real}(V_1)}{\sigma_n A_{app}} + \frac{(\tau_c(V_1) + \Delta\tau_c) \Delta A_{real}}{\sigma_n A_{app}} = \frac{\Delta\tau_c R(V_1)}{\sigma_n} + \frac{\tau_c(V_1) \Delta R}{\sigma_n}, \quad (A5)$$

where $R = A_{real}/A_{app}$ represents the ratio of the real contact area per apparent area.

The first term on the right of equation (A5) expresses a direct change in friction caused by the change in the shear stress at steady state contact area at V_1 (the direct effect), while the second term shows the change in the friction caused by the evolutionary change in the real contact area (the evolution effect). A constitutive law for friction controlled by asperity deformation has been derived by previous studies such as Brechet and Estrin [1994], Nakatani [2001], and Hatano [2015] adopting an exponential relationship,

$$V = V_r \exp\left(-\frac{E - \tau_c \Omega}{k_B T}\right), \quad (A6)$$

where E is the activation energy and V_r is a reference velocity scaled by a product of sound velocity and bond-reconnection strain at the asperity [Hatano, 2015]. From equation (A6), the shear stress increment $\Delta\tau_c$ supported at the asperities due to a velocity change from V_1 to V_2 is

$$\Delta\tau_c = \frac{k_B T}{\Omega} \ln\left(\frac{V_2}{V_1}\right). \quad (A7)$$

Inserting (A7) into (A5), and comparing with equation (1), we thus obtain a definitive expression of the direct effect (5), which is caused by both thermally activated processes and a change in real contact area, yielding

$$a = \frac{k_B T}{\Omega} \cdot \frac{R(V_1)}{\sigma_n}. \quad (A8)$$

Acknowledgments

All authors show greatly thanks to two anonymous reviewers for their fruitful comments. First author thanks Akira Owada and Takumi Sato for their outstanding dry-polish techniques on thin section preparation. This research was partially supported by JSPS KAKENHI, Grant-in-Aid for 25610150 (M. Takahashi), by the ERC starting grant SEISMIC (335915) (M. P. A. v. d. Ende) and by the Netherlands Organization for Scientific Research (NWO) through a VIDI grant (854.12.011) and by the ERC starting grant SEISMIC (335915) (A. Niemeijer). The authors have no financial conflict of interest. The experimental data are available from the corresponding author on request.

References

- Beeler, N. M., T. E. Tullis, M. L. Blanpied, and J. D. Weeks (1996), Frictional behavior of large displacement experimental faults, *J. Geophys. Res.*, **101**, 8697–8715, doi:10.1029/96JB00411.
- Blanpied, M. L., C. J. Marone, D. A. Lockner, J. D. Byerlee, and King (1998), Quantitative measure of the variation in fault rheology due to fluid-rock interactions, *J. Geophys. Res.*, **103**, 9691–9712, doi:10.1029/98JB00162.
- Bos, B., and C. J. Spiers (2000), Effect of phyllosilicates on fluid-assisted healing of gouge-bearing faults, *Earth Planet. Sci. Lett.*, **184**, 199–210.
- Bos, B., and C. J. Spiers (2002), Fluid-assisted healing processes in gouge-bearing faults: insights from experiments on a rock analogue system, *Pure Appl. Geophys.*, **159**, 2537–2566.
- Bos, B., C. J. Peach, and C. J. Spiers (2000a), Frictional-viscous flow of simulated fault gouge caused by the combined effects of phyllosilicates and pressure solution, *Tectonophysics*, **327**, 173–194.
- Bos, B., C. J. Peach, and C. J. Spiers (2000b), Slip behavior of simulated gouge-bearing faults under conditions favoring pressure solution, *J. Geophys. Res.*, **105**, 16,669–16,718.
- Brechet, Y., and Y. Estrin (1994), The effect of strain rate sensitivity on dynamic friction of metals, *Scr. Metall. Mater.*, **30**, 1449–1454.
- Demurtas, M., M. Fondriest, F. Balsamo, L. Clemenzi, F. Storti, A. Bistacchi, and G. Di Toro (2016), Structure of a normal seismogenic fault zone in carbonates: The Vado di Corno Fault, Campo Imperatore, Central Apennines (Italy), *J. Struct. Geol.*, **90**, 185–206, doi.org/10.1016/j.jsg.2016.08.004.
- Dieterich, J. H. (1972), Time-dependent friction in rocks, *J. Geophys. Res.*, **77**, 3690–3697.
- Dieterich, J. H. (1978), Time-dependent friction and the mechanics of stick-slip, *Pure Appl. Geophys.*, **116**, 790–806.
- Dieterich, J. H. (1979), Modeling of rock friction: 1. Experimental results and constitutive equations, *J. Geophys. Res.*, **84**, 2161–2168.
- Di Toro, G., T. Hirose, S. Nielsen, G. Pennacchioni, and T. Shimamoto (2006), Natural and experimental evidence of melt lubrication of faults during earthquakes, *Science*, **311**, 647–649, doi:10.1126/science.1121012.
- Handy, M. R., G. Hirth, and N. Hovius (2007), Continental fault structure and rheology from the frictional-to-viscous transition downward, in *Tectonic Faults: Agents of Change on a Dynamic Earth*, MIT Press, Cambridge, Mass.
- Hatano, T. (2015), Rate and state friction law as derived from atomistic processes at asperities, doi:arXiv:1512.05078 [cond-mat.stat-mech].
- Hobbs, B. E., A. Ord, and C. Teyssier (1986), Earthquakes in ductile regime?, *Pure Appl. Geophys.*, **124**, 309–336.
- Holdsworth, R. E., M. Stewart, J. Imber, and R. A. Strachan (2001), The structure and rheological evolution of reactivated continental fault zones: A review and case study, *Geol. Soc. Spec. Publ.*, **184**, 115–137, doi:10.1144/GSL.SP.2001.184.01.07.
- Ikari, M. J., D. M. Saffer, and C. Marone (2009), Frictional and hydrologic properties of clay-rich fault gouge, *J. Geophys. Res.*, **114**, B05409, doi:10.1029/2008JB006089.
- Jiang, H., C.-T. A. Lee, J. K. Morgana, and C. H. Rossa (2015), Geochemistry and thermodynamics of an earthquake: A case study of pseudotachylites within mylonitic granitoid, *Earth Planet. Sci. Lett.*, **430**, 235–248, doi:10.1016/j.epsl.2015.08.027.
- Kilian, R., R. Heilbronner, and H. Stünitz (2011), Quartz grain size reduction in a granitoid rock and the transition from dislocation to diffusion creep, *J. Struct. Geol.*, **33**, 1263–1284, doi:10.1016/j.jsg.2011.05.004.
- Lama, R. D., and V. S. Vutukuri (1978), *Handbook on Mechanical Properties of Rocks: Testing Techniques and Results*, vol. 2, pp. 495, Trans. Tech. Publ., Clausthal-Zellerfeld, Germany.

- Lapusta, N., and J. R. Rice (2003), Nucleation and early seismic propagation of small and large events in a crustal earthquake model, *J. Geophys. Res.*, **108**(B4), 2205, doi:10.1029/2001JB000793.
- Lapusta, N., J. R. Rice, Y. Ben-Zion, and G. Zheng (2000), Elastodynamic analysis for slow tectonic loading with spontaneous rupture episodes on faults with rate- and state-dependent friction, *J. Geophys. Res.*, **105**, 23,765–23,790, doi:10.1029/2000JB900250.
- Lin, A. (2008), *Fossil Earthquakes: The Formation and Preservation of Pseudotachylites*, 348 pp., Springer, Berlin, Heidelberg, New York.
- Logan, J. M., and L. W. Teufel (1986), The effect of normal stress on the real area of contact during frictional sliding in rocks, *Pure Appl. Phys.*, **124**, 471–485.
- Nakatani, M. (2001), Conceptual and physical clarification of rate and state friction: Frictional sliding as a thermally activated rheology, *J. Geophys. Res.*, **106**, 13,347–13,380, doi:10.1029/2000JB900453.
- Niemeijer, A. R., and C. J. Spiers (2005), Influence of phyllosilicates on fault strength in the brittle-ductile transition: Insight from rock analogue experiments, *Geol. Soc. Spec. Publ.*, **245**, 303–327.
- Niemeijer, A. R., and C. J. Spiers (2006), Velocity dependence of strength and healing behavior in simulated phyllosilicate-bearing fault gouge, *Tectonophysics*, **427**, 231–253.
- Niemeijer, A. R., and C. J. Spiers (2007), A microphysical model for strong velocity weakening in phyllosilicate-bearing fault gouges, *J. Geophys. Res.*, **112**, B10405, doi:10.1029/2007JB005008.
- Niemeijer, A. R., G. Di Toro, W. A. Griffith, A. Bistacchie, S. A. F. Smith, and S. Nielsen (2012), Inferring earthquake physics and chemistry using an integrated field and laboratory approach, *J. Struct. Geol.*, **39**, 2–36, doi:10.1016/j.jsg.2012.02.018.
- Noda, H., and T. Hori (2014), Under what circumstances does a seismogenic patch produce aseismic transients in the later interseismic period?, *Geophys. Res. Lett.*, **41**, 7477–7484, doi:10.1002/2014GL061676.
- Noda, H., and T. Shimamoto (2009), Constitutive properties of clayey fault gouge from the Hanaore fault zone, southwest Japan, *J. Geophys. Res.*, **114**, B04409, doi:10.1029/2008JB005683.
- Noda, H., M. Nakatani, and T. Hori (2013), Large nucleation before large earthquakes is sometimes skipped due to cascade-up: Implications from a rate and state simulation of faults with hierarchical asperities, *Geophys. Res. Solid Earth*, **118**, 2924–2952, doi:10.1002/jgrb.50211.
- Paterson, M. S. (1978), *Experimental Rock Deformation—The Brittle Field*, pp. 256, Springer, Berlin-Heidelberg.
- Reinen, L. A., J. D. Weeks, and T. E. Tullis (1994), The frictional behavior of lizardite and antigorite serpentinites: Experiments, constitutive models implications for natural faults, *Pure Appl. Geophys.*, **143**(1–3), 317–358, doi:10.1007/BF00874334.
- Rice, J. R., N. Lapsuta, and K. Ranjith (2001), Rate and state dependent friction and the stability of sliding between elastically deformable solids, *J. Mech. Phys. Solids*, **49**, 1865–1898.
- Rubin, A. M., and J.-P. Ampuero (2005), Earthquake nucleation on (aging) rate and state faults, *J. Geophys. Res.*, **110**, B11312, doi:10.1029/2005JB003686.
- Ruina, A. (1983), Slip instability and state variable friction laws, *J. Geophys. Res.*, **88**, 10,359–10,370, doi:10.1029/JB088iB12p10359.
- Sibson, R. H. (1975), Generation of pseudotachylite by ancient seismic faulting, *Geophys. J. R. Astron. Soc.*, **43**, 775–794.
- Sibson, R. H. (1980), Transient discontinuities in ductile shear zones, *J. Struct. Geol.*, **2**, 165–174.
- Sibson, R. H. (2003), Thickness of the seismic slip zone, *Bull. Seismol. Soc. Am.*, **93**, 1169–1178, doi:10.1785/0120020061.
- Smith, S. A. F., A. Billi, G. Di Toro, and R. Spiess (2011), Principal slip zones in limestone: Microstructural characterization and implications for the seismic cycle (Tre Monti Fault, Central Apennines, Italy), *Pure Appl. Geophys.*, **168**, 2365–2393, doi:10.1007/s00024-011-0267-5.
- Smith, S. A. F., S. Nielsen, and G. Di Toro (2015), Strain localization and the onset of dynamic weakening in calcite fault gouge, *Earth Planet. Sci. Lett.*, **413**, 25–36, doi:10.1016/j.epsl.2014.12.043.
- Smith, S. A. F., M. Demurtas, E. Spagnuolo, M. Fondriest, and G. Di Toro (2016), Coseismic origin of foliated cataclasites and preservation potential during the seismic cycle, Abstract S21B-2705 presented at 2016 AGU Fall Meeting, San Francisco, Calif., 12–12 Dec.
- Takagi, H., K. Goto, and N. Shigematsu (2000), Ultramylonite bands derived from cataclasite and pseudotachylite in granites, northeast Japan, *J. Struct. Geol.*, **22**, 1325–1339.
- Takahashi, M., S.-I. Uehara, K. Mizoguchi, I. Shimizu, K. Okazaki, and K. Masuda (2011), On the transient response of serpentine (antigorite) gouge to stepwise changes in slip velocity under high-temperature conditions, *J. Geophys. Res.*, **116**, B10405, doi:10.1029/2010JB008062.
- Van den Ende, M. P. A., G. Marketos, A. R. Niemeijer, and C. J. Spiers (2016), An investigation of the contribution of cohesion to interseismic restrengthening of fault gouges, paper presented at the 2016 Rock Deformation Gordon Research Conference, Proctor Academy, Andover, N. H.

Erratum

In the originally published version of this article, in the Acknowledgments, M. P. A. v. d. Ende's name was misspelled. The error has since been corrected and this version may be considered the authoritative version of record.